



Role of Direct Quenching and Partitioning Processes in Improving Austenite Stability and Stretch Flangeability in a Low C Steel

Chintada Umasankar¹ · Kali Prasad^{2,3} · Yeon Taek Choi⁴ · Do Won Lee⁴ · Hyung Seop Kim^{2,4,5} · S. Sankaran¹ · Uday Chakkingal¹

Received: 23 May 2024 / Accepted: 28 June 2024

© The Author(s) under exclusive licence to The Korean Institute of Metals and Materials 2024

Abstract

The current research work introduces a novel processing technique involving a combination of hot rolling and a direct quench and partitioning treatments to produce an ultra-high strength, low-carbon and lean-composition steel with superior mechanical properties and enhanced stretch flangeability. The methodology involves the introduction of a secondary partitioning step after a one-step direct quenching and partitioning (DQP) process. A detailed investigations on microstructures, tensile properties and stretch flangeability (using hole expansion testing) were carried out. The martensite-austenite two phase microstructure resulted in a remarkably improved product of strength and elongation (PSE, 24 GPa.%), the hole expansion ratio of 45% and a total elongation of 21.7%. It is shown that the stability of retained austenite, rather than its volume fraction, has a significant impact on the strain hardening rate, and therefore influences strength, ductility and stretch flangeability. The results indicate that tailoring retained austenite stability is essential for optimizing the mechanical performance and stretch flangeability of quenched and partitioned steels. Introducing secondary partitioning into the Q&P process provides a feasibility to achieve a large fraction of total retained austenite, (predominantly film-type, along with small-sized blocky retained austenite islands in the microstructure), which results in high-strength Q&P steels with excellent global and local formability.

Keywords Quenching and partitioning steels · Austenite · Formability · Secondary partitioning

1 Introduction

Quenched and Partitioned (Q&P) steels are a class of third-generation advanced high strength steels (AHSS). Achieving high strength and ductility with a lean-composition while maintaining adequate formability still remains a challenge. The primary objective of the Q&P treatment is to achieve a desirable amount of stable retained austenite (RA) in the microstructure by increasing the carbon content within RA via carbon partitioning from martensite to austenite. Various Q&P techniques have been employed, such as single-step Q&P [1, 2], two-step Q&P [3, 4], Q&P-tempering (Q-P-T) [5], Bainitic-Q&P (B-QP) [6, 7], and direct Q&P (DQP) [8–10]. In comparison to conventional Q&P, the DQP has attracted significant research interest for its ability to achieve high strength and sufficient ductility in low-carbon and lean-composition steels. Using a combination of hot rolling with Q&P treatment (i.e., DQP), Xiaodong Tan et al. [8] reported ultimate tensile strength (UTS) values of 1500–1600 MPa and total elongation (TE) values

✉ Uday Chakkingal
udaychak@iitm.ac.in

¹ Department of Metallurgical and Materials Engineering, Indian Institute of Technology Madras, Chennai 600036, India

² Graduate Institute of Ferrous and Eco Materials Technology (GIFT), Pohang University of Science and Technology (POSTECH), Pohang 37673, Republic of Korea

³ Department of Mechanical Engineering, Indian Institute of Technology Madras, Chennai 600036, India

⁴ Department of Materials Science and Engineering, Pohang University of Science and Technology (POSTECH), Pohang 37673, Republic of Korea

⁵ Institute for Convergence Research and Education in Advanced Technology, Yonsei University, Seoul 03722, Republic of Korea

of 14–16%. By controlling hot rolling parameters, Parthiban et al. [10] achieved superior UTS values of 1593 MPa and TE values of 13% in CMnSiAl DQP steel.

To withstand sheet metal stamping operations and prevent edge cracking, good stretch flangeability is essential. Stretch flangeability is usually measured using the hole expansion test (HET) where a standard specimen with a hole of 10 mm diameter is taken, and the hole is expanded by a conical punch. The percentage increase in hole diameter is referred to as the hole expansion ratio (HER) and this value is a measure of the stretch flangeability of the sheet. HER values have been correlated to tensile properties, even though uniaxial tensile testing has a different deformation mode compared to HET. These properties include UTS [11–14], post-uniform elongation [15, 16], yield ratio (yield strength (YS)/UTS) [17], and strain hardening rate [18]. In addition, various factors have been proposed to explain stretch flangeability, including the volume fraction and stability of RA in TRIP-assisted steel [19], the discrepancy in hardness between the hard and soft phases in multi-phase steel [20, 21], and the size of the shear-affected-zone (SAZ) induced by hole punching [22]. However, limited efforts have been made to assess the stretch flangeability of Q&P steels, which is essential for industrial use.

Some of these methodologies were used to study the stretch flangeability of Q&P heat-treated steel [23–28]. Kim et al. [25] performed a two-step Q&P on medium Mn steel and identified prior austenite grain size and RA morphology as critical factors affecting stretch flangeability (HER of 18.1–38%). Im et al. [26] studied the influence of microstructure on the stretch flangeability of Fe-0.18 C-1.5Si-2.6Mn-0.05Al steel under different Q&P and Q&P-T conditions

and, reported an improvement in HER (17.3–33.6%) via Q&P-T. Recently, Toji et al. [27] applied two-step Q&P treatment to low-carbon steel, resulting in improved total elongation (TE = 15.4%) and a greater hole expansion ratio (40%) than conventional TRIP steel with the same tensile strength (approximately 1200 MPa). The reason was ascribed to a microstructure comprised of a lower volume fraction of large blocky martensite, a higher inter-lath film-type RA fraction, and bainitic ferrite.

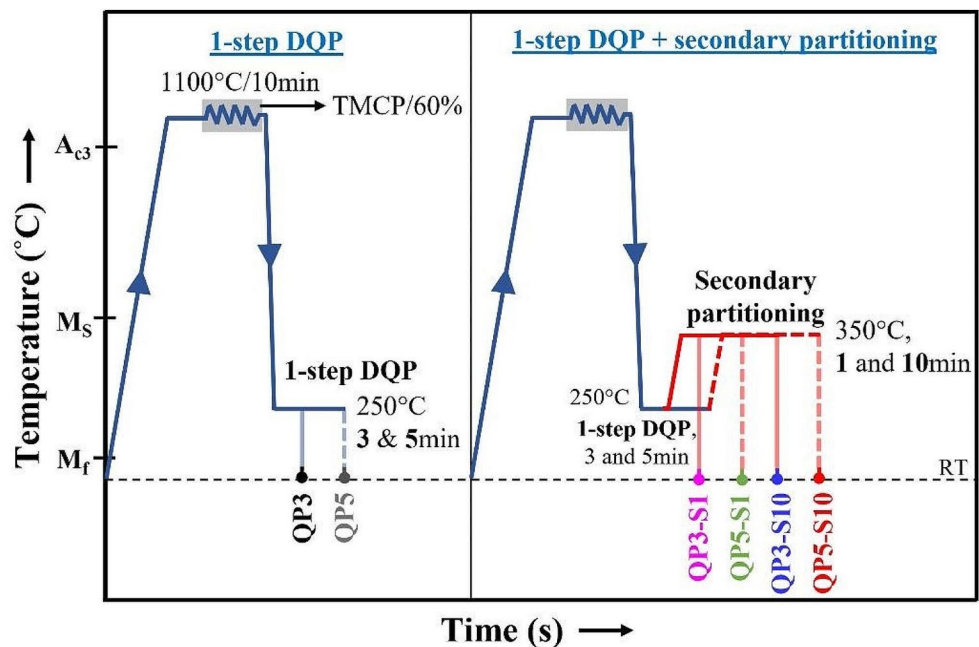
In the current study, a one-step DQP treatment followed by a new secondary partitioning step, was introduced immediately after hot-rolling to produce an ultra-high-strength Q&P steel with superior tensile properties and HER. The RA stability was studied through interrupted tensile tests as function of strain. In addition, the influence of secondary partitioning was extensively studied by examining the correlation between tensile properties, HER, RA fraction, and its stability.

2 Experimental Procedures

2.1 Processing Method of DQP

The investigated steel has a chemical composition of Fe-0.26 C-1.87Mn-0.99Al-0.45Si (wt%). For DQP investigations, steel specimens with dimensions of $35 \times 30 \times 3.5$ mm³ (length \times width \times thickness) were machined using milling and surface grinding. Figure 1 depicts the thermal cycle for DQP heat treatments. The process treatments included austenitization at 1100 °C for 10 min in a high-temperature box furnace followed by controlled hot rolling up to a 60%

Fig. 1 Schematic of processing schedule involving hot-rolling and direct quenching and partitioning (DQP) and secondary partitioning treatments



reduction in thickness over four passes in a laboratory rolling mill with a finish rolling temperature ranging between 970 °C and 1010 °C. After hot rolling, the one-step direct Q&P was then performed. The specimens were immediately quenched in a salt bath furnace at 250 °C for 3 and 5 min, subsequently water quenched to room temperature. Some specimens were also subjected to secondary partitioning treatments, wherein, specimens after quenching and partitioning at 250 °C for 3 and 5 min were reheated to 350 °C for 1 and 10 min in a salt bath furnace and subsequently quenched in water. Specimens produced by one-step Q&P at 250 °C for 3 and 5 min are termed hereafter as QP3 and QP5, respectively. Specimens produced by one-step Q&P at 250 °C for 3 and 5 min followed by secondary partitioning step at 350 °C for 1 and 10 min of each QP3 and QP5 samples are termed hereafter as QP3-S1, QP3-S10, QP5-S1, and QP5-S10, respectively. The selection of heat treatment windows is arrived at based on our earlier studies [3, 9].

2.2 Microstructural Characterization

2.2.1 Electron Microscopy

(a) Specimen preparation:

For SEM analysis, the specimens were manually polished to P2500 grit SiC paper. The specimens were electropolished at -10 °C using A2-electrolyte (720 ml ethanol, 120 ml butoxy ethanol, 80 ml distilled water, and 80 ml perchloric acid) using Struers Lectropol-5. A voltage of 10 V was applied during the process to obtain a scratch-free surface. For EBSD studies, specimens were mechanically ground up to P4000 grit emery sheet, then polished with 3 μm diamond paste. The final polishing was carried out with a 70% colloidal silica suspension (0.05 μm particle size) and 30% hydrogen peroxide solution. For TEM specimen preparation, steel foils were punched into 3 mm discs from mechanically polished 100 μm thick foils, followed by twin-jet electropolishing (Struers Tenupol-5) using 90% CH₃OH and 10% HClO₄ at -30 °C. In addition, the fractured portion of the post-mortem tensile specimens was sliced vertically, and ~3 mm discs were cut along the gage length. The discs were made from the region just below the fracture surface.

(b) Testing method and analysis:

The specimens were examined under FEG SEM (Apreo S, ThermoFisher make) and a thermionic SEM (Inspect F, FEI make) operating at a voltage of 25 kV. EBSD scans were carried out in FEG SEM (Apreo-S, ThermoFisher make) with an accelerating voltage of 25 kV, with a step size of 50 nm, and the data was acquired using a high-speed camera (model Velocity, EDAX make). The TSL-OIM software was used to post-process the acquired data. TEM

investigations were performed on Tecnai-20 (ThermoFisher make) with an acceleration voltage of 200 kV.

2.2.2 X-ray Diffraction Analysis

The volume fractions of different phases were determined by X-ray diffraction (XRD, Bruker AXS D8 Discover X-ray diffractometer, operated at 30 kV) analysis with Co K_α radiation from the integrated intensities of the monitored peaks including (200)_α, (211)_α, (200)_γ, and (220)_γ. The detailed procedure for determining the RA volume fraction can be found in Ferreira et al. [29]. The percentage of carbon in RA was determined by substituting the lattice parameter value obtained through Rietveld refinement (X'Pert High Score Plus Rietveld refinement software) into the following Eq. (1) [30, 31].

$$a_{\gamma} (\text{Å}) = 3.556 + 0.0453w_C + 0.00095w_{Mn} + 0.0056w_{Al} \quad (1)$$

where w_C , w_{Mn} , and w_{Al} are the composition of carbon, manganese, and aluminum (in wt%), respectively in RA, and a_{γ} is the lattice parameter in Angstrom.

2.3 Evaluation of Tensile Properties

The uniaxial tensile tests were conducted using a universal tensile testing machine (Zwick/Roell Z100 100 kN), at an initial strain rate of $1 \times 10^{-3} \text{ s}^{-1}$. The flat dog-bone shaped specimens were machined parallel to the rolling direction, according to the ASTM E 8 M [32], with a gauge length of 25 mm, a width of 3 mm and a thickness of 1 mm. Three tensile tests were performed for each DQP condition, and the average values of tensile properties together with their standard deviation were determined. The strain hardening rate (θ) is estimated for the multi-stage hardening behaviors, according to Eq. (2).

$$\theta = d\sigma/d\epsilon \quad (2)$$

where σ is true stress and ϵ is true strain. In addition, interrupted tensile tests were carried out to different strains to examine the RA stability in the light of TRIP effect.

2.4 Hole Expansion Testing

HETs were carried out using a scaled-down HET setup [33, 34], mounted on a universal testing machine. Circular specimens of 10 mm in diameter with an initial hole diameter of 2 mm punched at their center and a thickness of 0.5 mm were prepared from the sheet. Before punching, the circular specimen surfaces were mechanically polished using SiC papers with grit sizes ranging from 600 to 1200 to minimize

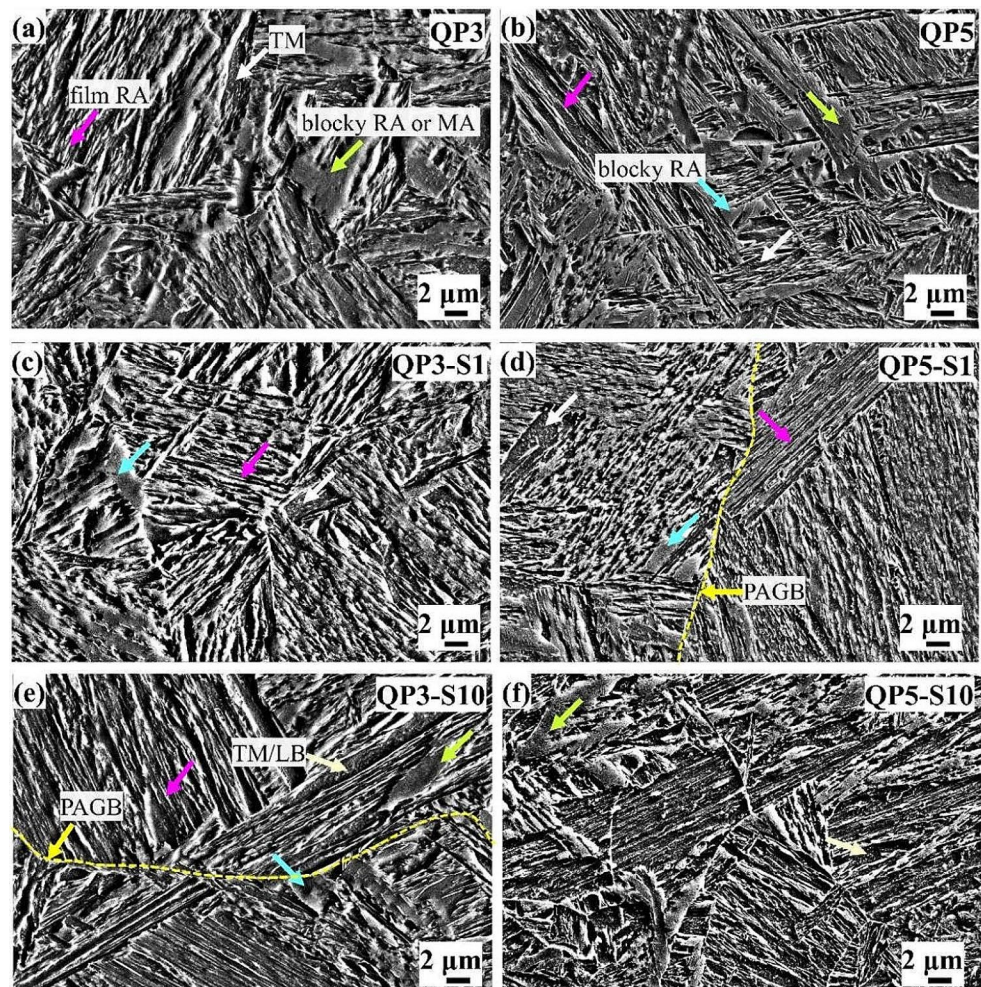
surface roughness. The HETs were performed at a consistent punch velocity of 1 mm/min. Testing was stopped once the hole edge crack propagated completely through the thickness. After the testing, the final hole diameters were measured. The HER was determined using the following Eq. (3) [35]:

$$HER(\%) = \frac{d_f - d_0}{d_0} \times 100 \quad (3)$$

where d_0 and d_f are the initial and final hole diameters, respectively. The HER was calculated by averaging the results of five tests conducted on each DQP specimen.

The shear-affected zone (SAZ) analysis resulting from punching process was conducted on QP5, QP5-S1, and QP5-S10 samples by examining hardness profiles. Micro Vickers hardness testing, employing an applied load of 0.5 kgf, was performed using an Innovatest Falcon 600 apparatus. Hardness measurements were taken at intervals of 100 μm along the interface between the burnished and fractured sections. Five measurements were averaged to derive the reported values.

Fig. 2 SEM micrographs of (a) QP3, (b) QP5, (c) QP3-S1, (d) QP5-S1, (e) QP3-S10, and (f) QP5-S10 containing tempered martensite (TM), retained austenite (RA), fresh martensite/austenite (MA) islands, and TM or lower bainite (TM/LB). A prior austenite grain boundary (PAGB) is also highlighted

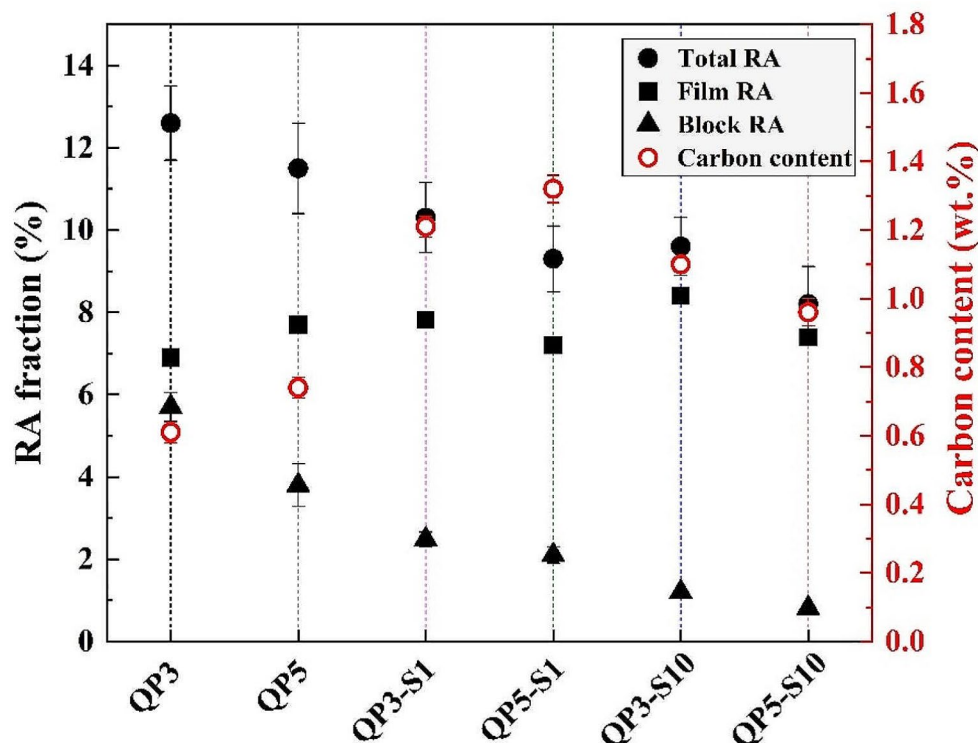


3 Results

3.1 Microstructure Changes During the Heat Treatment Process

The typical microstructures of Q&P steels subjected to single-step partitioning and secondary partitioning are depicted in Fig. 2. Figure 2a and b depict SEM micrographs of QP3 and QP5, displaying constituents including tempered martensite, RA, and fresh martensite-austenite (MA) islands. Fresh martensite is formed through the transformation of metastable RA during the final quenching to room temperature. When the partitioning time increases from 3 to 5 min, the total RA fraction decreases from 12.6 to 11.5%, and its carbon content increases from 0.61 to 0.74 wt% (Fig. 3). This steel has RA in both blocky and film-type. The film-type RA occurs predominantly between martensitic laths, whereas blocky RA islands are predominantly found along the boundaries of martensitic packets. The total amount of RA is measured by XRD, and ImageJ software was used to manually estimate the blocky RA fraction from SEM images. The film-type RA fraction is then calculated by

Fig. 3 The evolution of RA fraction and carbon content for the single-step partitioned (QP3, QP5), and secondary partitioned (QP3-S1, QP5-S1, QP3-S10, and QP5-S10) DQP steels



subtracting the blocky RA fraction from the total RA fraction. Increasing partitioning time from 3 to 5 min results in an increase in the film-type RA fraction from 6.9 to 7.7% and significant decrease in the blocky RA fraction from 5.7 to 3.8% (Fig. 3). Furthermore, the size of blocky RA is dependent on partitioning time with its size decreasing with an increase in partitioning time. On increasing partitioning time from 3 to 5 min, the equivalent circle diameter (ECD) of blocky RA islands decreases from $2.82 \pm 0.18 \mu\text{m}$ for QP3 to $2.1 \pm 0.03 \mu\text{m}$ for QP5.

Similarly, the specimens subjected to secondary partitioning primarily comprise a matrix of tempered martensite and RA (Fig. 2(c-f)). When the secondary partitioning time increases from 1 min to 10 min, the total RA fraction decreases from 10.3 to 8.2%, and the carbon content of RA decreases from 1.21 to 0.96 wt%. In addition to the microconstituents mentioned above, the final microstructure of QP3-S10 and QP5-S10 specimens also consists of small amount of lower bainite ($\sim 0.5\%$), which is a product of the partitioning process at 350°C for extended durations, specifically for 10 min. Additionally, this extended partitioning leads to the substantial substitution of fresh martensite with tempered martensite. As the secondary partitioning time is increased from 1 to 10 min, the fraction of film-type RA increases by approximately 30% (Fig. 3). It is worth noting that the fraction of film-type RA ranges 7.3~8.5% in secondary partitioned specimens partitioned for 10 min, indicating that the film morphology is the predominant shape. Additionally, the size of the blocky RA is dependent on the

secondary partitioning time with its size decreasing with an increase in partitioning time. On increasing secondary partitioning time from 1 to 10 min, the ECD of blocky RA islands significantly decreases for secondary partitioned specimens, e.g., the ECD of blocky RA islands decreases from $1.16 \pm 0.21 \mu\text{m}$ for QP5-S1 to $0.78 \pm 0.18 \mu\text{m}$ for QP5-S10.

3.2 Uniaxial Tensile Properties and HER

Figure 4 shows the engineering stress-engineering strain curves (Fig. 4a) and the hole expansion ratios (Fig. 4b) of Q&P steels subjected to single-step partitioning and secondary partitioning heat treatments. Table 1 summarizes the results of uniaxial tensile and hole expansion tests. All the DQP-processed specimens show continuous yielding behaviour (Fig. 4a). The QP5-S10 specimen achieves excellent tensile properties with YS of 792 MPa, UTS of 1122 MPa, TE of 21.7% and PSE of 24.3 GPa·%, also exhibiting highest stretch flangeability (HER=45%). Whereas the QP3-S10 specimen shows UTS of 1136 MPa, TE of 19.3% and HER of 36%, and QP3 specimen exhibit high strength of 1370 MPa but low TE of 10.4%, and poor HER (22%). Both UTS and ductility (TE and HER) are significantly influenced by the secondary partitioning process, the change in Q&P treatment from one-step Q&P to secondary partitioning promotes TE and HER with a reduction in UTS.

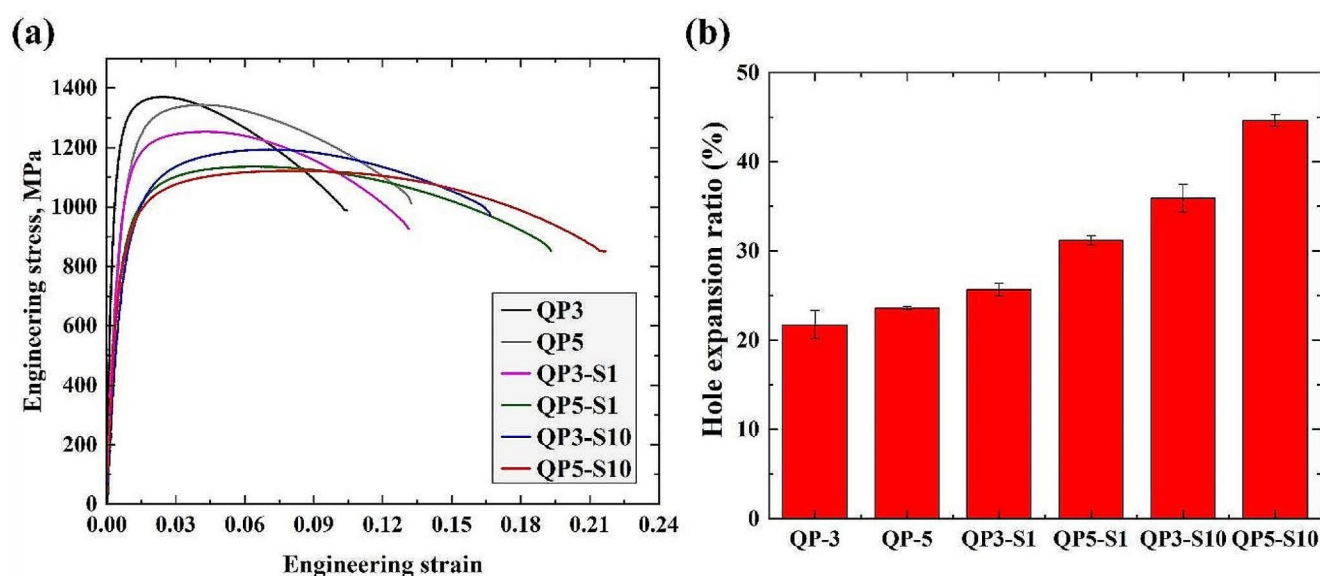


Fig. 4 (a) Engineering stress-strain curves, and (b) hole expansion ratios of the DQP-processed steels

Table 1 Mechanical properties of DQP-processed specimens from uniaxial tensile and hole expansion tests

Notation	YS (MPa)	UTS (MPa)	UE (%)	TE (%)	PSE (GPa.%)
QP3	1052 ± 34	1370 ± 17	2.4 ± 0.9	10.4 ± 2.1	14.3
QP5	1048 ± 13	1344 ± 15	4.2 ± 0.6	13.2 ± 1.6	17.8
QP3-S1	930 ± 24	1253 ± 11	4.2 ± 0.3	13.1 ± 1.8	16.5
QP5-S1	803 ± 31	1193 ± 15	7.0 ± 1.3	16.7 ± 0.9	19.9
QP3-S10	773 ± 28	1136 ± 29	6.5 ± 0.2	19.3 ± 1.0	21.9
QP5-S10	792 ± 16	1122 ± 12	8.1 ± 0.4	21.7 ± 1.3	24.3

YS: 0.2% yield strength; UTS: ultimate tensile strength; UE: uniform elongation; TE: total elongation; PSE: product of strength and elongation

4 Discussion

4.1 The Dependence of Tensile Properties on RA Stability

The results of RA evolution (Fig. 3) and the mechanical properties of all specimens (Table 1) indicate that the QP3 specimen, which has the highest volume fraction of RA, does not exhibit superior mechanical properties, which is consistent with reports from the literature [23, 36]. Conversely, QP3-S10 and QP5-S10 specimens exhibit an excellent strength-ductility combination despite having a lower volume fraction of RA (Fig. 3). The results conclusively demonstrate that a certain amount of stability of RA is critical; too rapid deformation-induced transformation of RA into martensite is not conducive to a high strength-ductility combination. Thus, the results of these investigations can be explained based on the microstructure and stability of RA.

The crucial role of RA stability in influencing mechanical behavior is further investigated through: (i) interrupted tensile tests and XRD analysis, (ii) quantification of RA transformation rates in different initial microstructures using a mathematical equation proposed by Sugimoto et al. [37], and (iii) examination of the microstructure to understand the influence of RA transformation on strain hardening rates.

Figure 5a displays the strain hardening rate of DQP specimens, while Fig. 5b displays the evolution of RA fraction with increasing strain. In QP3 and QP5 specimens, the austenite fraction decreased from approximately 12–6%, indicating that over 50% of RA grains transform into martensite early during deformation (0.01 strain). Specifically, QP5 demonstrates a rapid decrease in strain hardening rate, and RA fraction reduced from 11.5 to 4.8% at 0.02 strain, indicating a lower TRIP effect. In contrast, when the strain increased from 0 to 0.01 in QP3-S1 and QP5-S1, only 2% RA was transformed into martensite. This transformation is accompanied by a notable increase in strain hardening rate after the initial drop (stage 1), indicating a substantial TRIP effect. Nevertheless, it is worth noting that around 4% RA remains even after failure, indicating that the RA was exceedingly stable and did not contribute to ductility via the TRIP effect. Furthermore, QP3-S10 and QP5-S10 exhibit a relatively smaller increase in strain hardening rate (stage 2) than QP3-S1 and QP5-S1, eventually declining gradually (stage 3). Notably, the gradual reduction in RA fraction with increasing strain, as shown in the Fig. 5b, is consistent with typical behavior observed in earlier studies [38, 39]. These results suggest that the evolution of strain hardening rate is influenced by the TRIP effect, which in turn depends on the

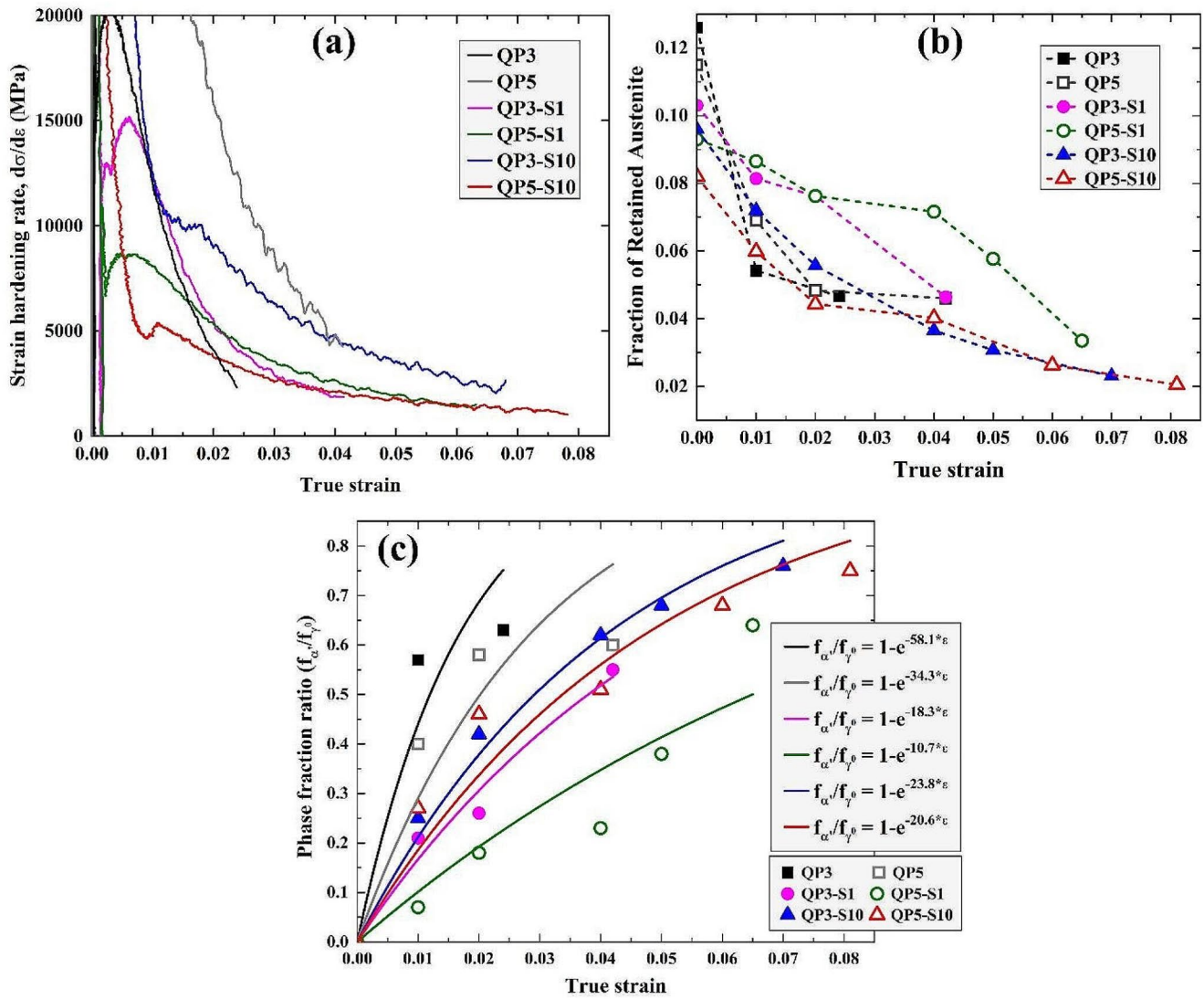


Fig. 5 (a) Strain hardening rate versus true strain, (b) the evolution of RA fraction as a function of true strain, and (c) the phase fraction ratio, $f_{\alpha'}/f_{\gamma^0}$ plotted as function of true strain: f_{γ^0} , $f_{\alpha'}$ and 'K' represent the initial RA fraction, the volume fraction of deformation-induced martensite at the specific true strain ϵ , and the stability parameter

mechanical stability of RA. However, in the current study, high strain hardening rates do not translate into higher PSE.

Sugimoto et al. [37] presented a mathematical formula for assessing the mechanical stability of RA during deformation in specimens with different initial microstructures.

$$\frac{f_{\alpha'}}{f_{\gamma^0}} = 1 - e^{-K\epsilon} \tag{4}$$

where f_{γ^0} , $f_{\alpha'}$ and 'K' represent the initial RA fraction, the volume fraction of deformation-induced martensite at the specific true strain ϵ , and a stability parameter inversely proportional to the stability of RA, respectively. The parameter 'K' (Fig. 5c) is an indicator of the rate of transformation of

inversely proportional to the stability of RA, respectively. The data points represent experimentally measured values, while the continuous lines indicate a fit to the mathematical equation $f_{\alpha'}/f_{\gamma^0} = 1 - e^{-K\epsilon}$, with the specific equations for each investigated condition indicated within the figure

RA. QP5-S1 had the lowest 'K' value of 10.7, while QP3 had the highest value of 58.1. Higher 'K' value indicates a more rapid austenite-to-martensite transformation, indicating lower RA stability. In contrast, a lower 'K' value indicates a delayed transformation rate and increased RA stability. Consequently, the RA of QP5-S1 was more stable during tensile deformation than that of QP3. Moreover, the findings indicate that mechanical performance is significantly affected by the extent of progressive transformation of RA. The stability of RA in DQP microstructure is a factor that warrants consideration. The different types of stability of RA in the current investigation are categorized based on the phase fraction, morphology, and size of RA, and stability parameter 'K' are summarized in Table 2. When a

Table 2 Parameters quantifying stability of retained austenite

Notation	Before deformation					After deformation		K	Stability of RA
	Film RA (%)	Block RA (%)	Total RA (%)	C (wt%)	ECD (μm)	Total RA (%)	C (wt%)		
QP3	6.9	5.7 ± 0.35	12.6 ± 0.9	0.61 ± 0.03	2.82 ± 0.18	4.66 ± 0.71	1.36 ± 0.04	58.1	Unstable
QP5	7.7	3.8 ± 0.52	11.5 ± 1.1	0.74 ± 0.03	2.1 ± 0.03	4.6 ± 0.92	1.31 ± 0.03	34.3	
QP3-S1	7.82	2.48 ± 0.18	10.3 ± 0.85	1.21 ± 0.03	1.42 ± 0.05	4.63 ± 0.79	1.62 ± 0.04	18.3	Exceedingly stable
QP5-S1	7.2	2.1 ± 0.19	9.3 ± 0.8	1.32 ± 0.04	1.16 ± 0.2	3.33 ± 0.82	1.51 ± 0.05	10.7	
QP3-S10	8.4	1.2 ± 0.07	9.6 ± 0.71	1.1 ± 0.02	0.84 ± 0.12	2.3 ± 1.2	1.23 ± 0.03	23.8	Stable
QP5-S10	7.39	0.81 ± 0.07	8.2 ± 0.92	0.96 ± 0.04	0.78 ± 0.18	2.05 ± 1.34	1.14 ± 0.03	20.6	

RA: Retained Austenite; ECD: Equivalent Circle Diameter; K: Stability Parameter; C: Carbon in RA

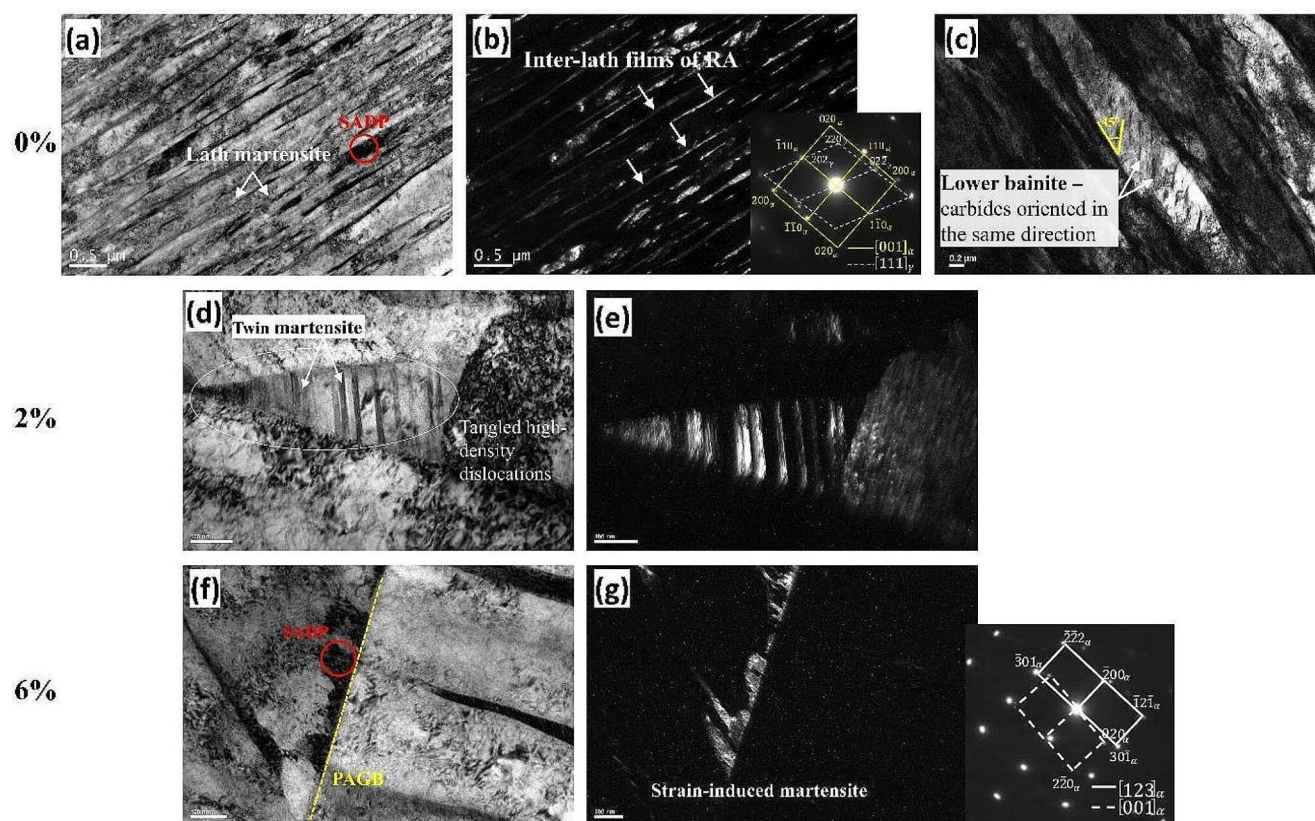


Fig. 6 (a) TEM micrographs of QP5-S10 samples during uniaxial tension interruption at engineering strains of (a, b, c) 0%, (d, e) 2%, and (f, g) 6%

microstructure consists solely of unstable RA, as seen in QP3 and QP5, the austenite undergoes quick transformation at low strains. Consequently, at high strain levels, the TRIP mechanism fails to offer sufficient strain hardening to postpone the initiation of necking. With an exceedingly stable RA, as observed in QP3-S1 and QP5-S1, a large fraction of RA does not effectively contribute to TRIP, resulting in suboptimal PSE. In the interim, an optimal microstructure (QP3-S10 and QP5-S10) with stable RA which is predominantly of film-type along with small-sized blocky RA can promote strain hardening rate in the initial stages of plastic deformation and contribute to an increase in PSE.

4.2 Transformation Activity of RA

Figure 6 depicts the martensite morphology of QP5-S10 under varying tensile strain levels. The film-type RA (~ 100 nm width) is evident between martensite laths (Fig. 6a, b). At 2% strain, twin martensite appears within lath martensite (Fig. 6d) with a thin plate width of approximately 15 nm, resulting from the transformation of film-type RA, which is consistent with prior research [40]. At 6% strain, strain-induced martensite is observed at the prior austenite grain boundary (PAGB) (Fig. 6f). However, at 2% and 6% strain, the lath martensite blurs due to interface migration between adjacent martensite laths under certain strain conditions, which is consistent with prior observations [40].

The transformation of film-type RA between martensite laths relieves stress concentration, preventing microcrack generation and propagation, thereby enhancing steel ductility.

Figure 7 illustrates the morphology of RA and twin martensite in QP5-S1 at different strain levels. At 2% strain, plastic deformation occurs preferentially in blocky-type RA grains. Twin martensite within martensite blocks is observed at 2% and 6% strain (Fig. 7c and e), indicating the transformation of RA within martensite blocks, which is consistent with prior research [40]. For RA within martensite blocks, the TRIP effect occurs preferentially in the interior of the RA, maintaining the interface and connecting martensite with twin martensite during deformation. This is a kind of buffering effect that contributes to deformation continuity, leading to decreased ductility. Furthermore, during straining, the interface accommodates plasticity between twin martensite and martensite blocks [40]. Additionally, the appearance of broken segments of inter-lath austenite films

indicate that inter-lath austenite films of RA are highly resistant to strain-induced transformation even after 6% strain. These exceedingly stable inter-lath films of RA do not effectively contribute to deformation, leading to suboptimal PSE.

In contrast, the QP5 specimen frequently displays coarse fresh martensite or blocky type RA (see Fig. 8a). Upon straining to failure, the deformed regions contain lath martensite with wavy boundaries, possibly due to the strain-induced martensite transformation (TRIP effect). Previous studies revealed that large blocks of RA are less stable and can undergo transformation into martensite even at minor strains, whereas thin austenite films are more stable and only transform into martensite at high strains [41]. The absence of blocky RA in Fig. 8c suggests that a large portion has been transformed into thin plate martensite. Additionally, the broken segments of coarse martensite/RA indicate that the coarse MA islands in QP5 appears to be unstable, hence

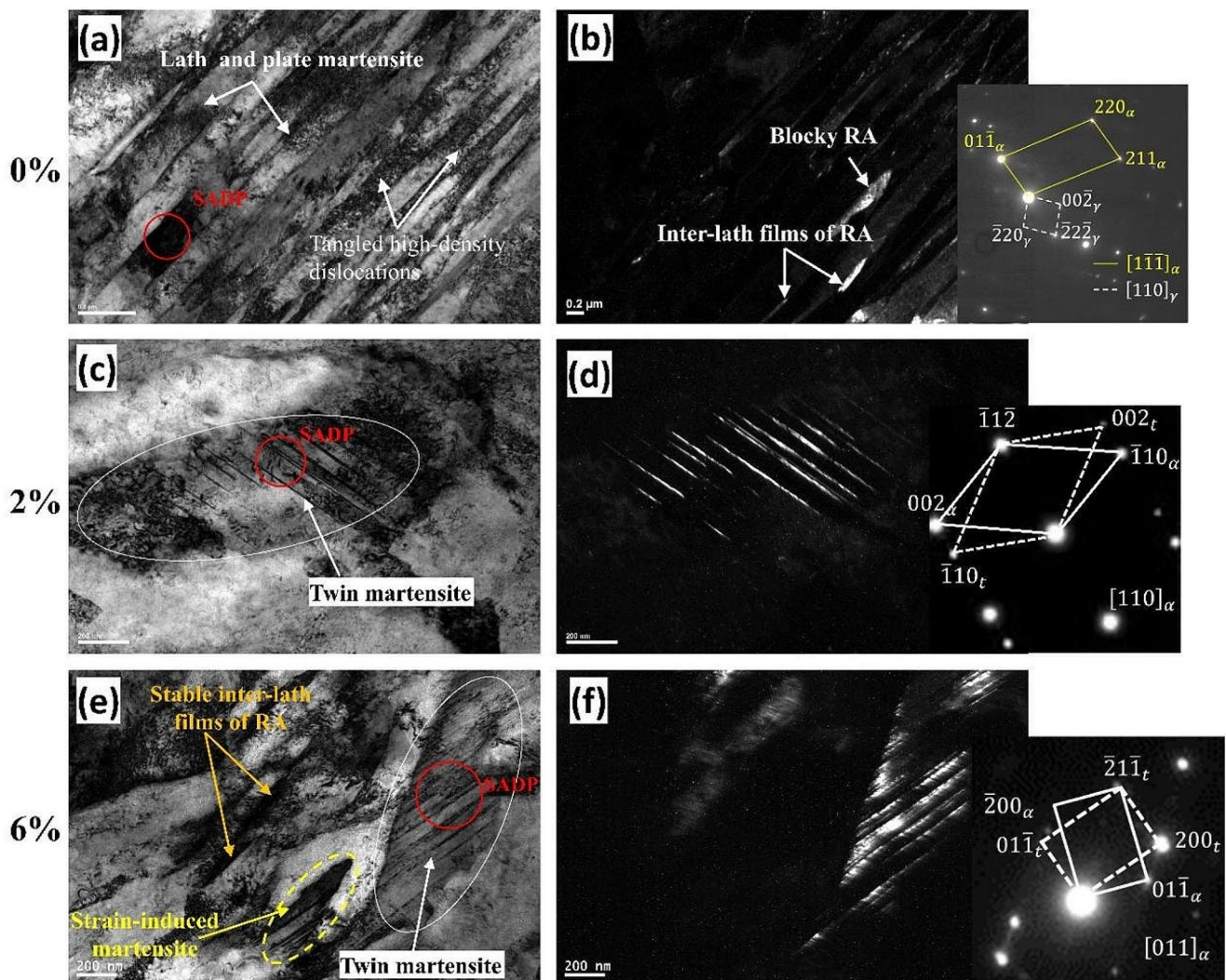
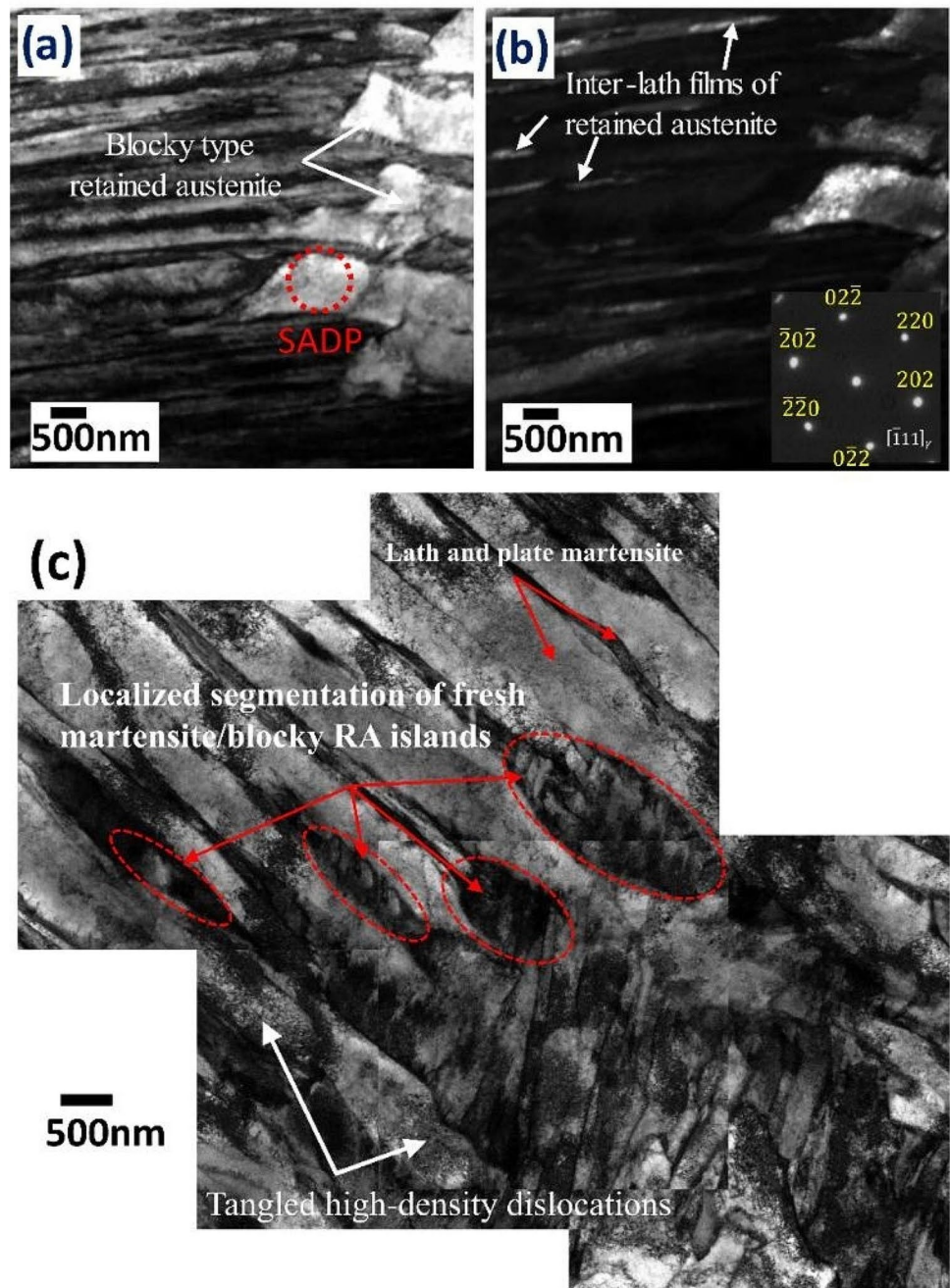


Fig. 7 (a) TEM micrographs of QP5-S1 samples during uniaxial tension interruption at engineering strains of (a, b) 0%, (c, d) 2%, and (e, f) 6%

Fig. 8 (a, b) Bright field TEM micrographs and dark field images with SAD pattern of QP5, where inter-lath films and pools of blocky type RA are indicated by arrows, and (c) a collage of TEM images of the QP5 steel after uniaxial tensile testing displays localized segmentation of coarse fresh martensite/RA islands



not effectively participating in the deformation ultimately leading to lower PSE.

Based on the above discussion, the influence of secondary partitioning time on RA evolution and its stability is significant. Especially at longer secondary partitioning times (QP3-S10 and QP5-S10), the microstructure with stable RA, which is predominantly film-type along with small-sized blocky RA, can promote strain hardening rate in the initial stages of plastic deformation and contribute to an increase in PSE. Therefore, introducing secondary partitioning to the DQP processing route of the studied low-carbon lean

alloy steel, resulting in an excellent combination of tensile properties and promising strain hardening response which encouraged the authors to investigate local formability, a crucial aspect of manufacturing and industrial applications.

4.3 Global and Local Formability Ensured by Secondary Partitioning

4.3.1 Hole Expansion Behavior

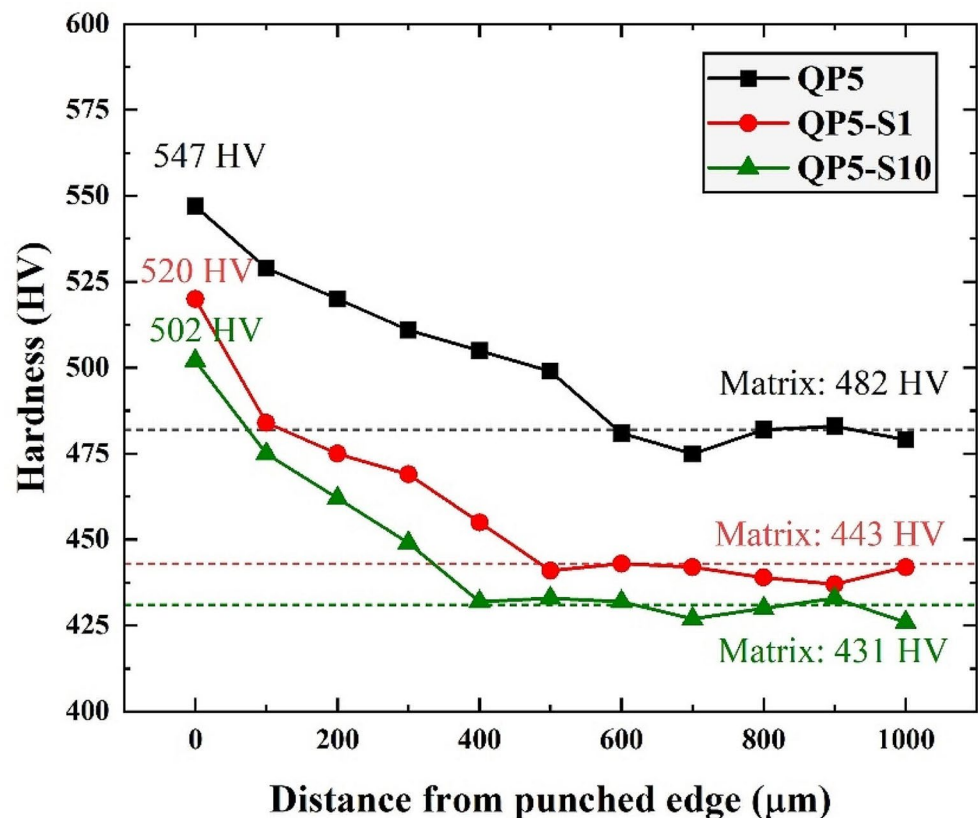
A large fraction of RA with dominant blocky morphology, such as in single-step DQP steels, can ensure good global formability but deteriorate local formability, which many Refs [36, 42–45] typically demonstrate. This explains why edge cracking occurs frequently during edge-stretching processes even when TE is sufficiently high [41, 42]. Reducing blocky RA fraction prevents this edge cracking, but it also lowers the total RA fraction, which reduces global formability [42, 44]. Instead of a single-step Q&P, the current investigation employs a secondary partitioning process followed by single-step Q&P. This results in a substantial total RA fraction, primarily of film-type together with small-sized blocky RA islands, which signifies good global formability (i.e. high PSE) and local formability (i.e. larger post-uniform elongation (TE-UE)).

HER of DQP specimens obtained using the conical HET with punched holes are shown in Fig. 4b. When compared to the other DQP steels, the QP3-S10 and QP5-S10 steels, which have lower strength levels and higher elongations, exhibit superior stretch flangeability. It may be inferred that the HER is proportionate to the total percentage elongation since the QP3 steel exhibits the lowest hole expansion in

relation to the lowest elongation. In the current work, there is a controversial effect of the RA stability which negatively contributes to the stretch flangeability. Stretch flangeability is negatively affected by both the greater RA fraction and the exceedingly stable RA.

The complete hole expansion experiment comprises two distinct stages: punching and hole expansion. The SAZ is a pre-damaged region resulting from the punching process employed to prepare HET specimens. Typically, SAZ is determined using the hardness profile from the punched hole edge [25]. This hardness profile exhibits a consistent decrease from the hole edge, reaching near constancy within the unaffected matrix beyond the SAZ boundary (Fig. 9). The unaffected matrix examined in specimens QP5, QP5-S1, and QP5-S10 had respective hardness values of 482 Hv, 443 Hv, and 431 Hv (Fig. 9). DQP specimens show a hardness increase of 50–70 Hv at the very edge of the hole due to strain-induced martensite formation during punching. For instance, in QP5 with a high RA of about 0.12, a significant increase in hardness (~70 Hv) in SAZ is due to more strain-induced martensite formation. As a damaged region, the SAZ influences early failure during HET, with smaller SAZ dimensions leading to higher HER values. Notably, QP5-S10 with RA of 0.08 corresponds to a smaller SAZ dimension (~350 μm) compared to QP5 with a high amount of RA 0.12 (~600 μm), resulting in a higher HER (Fig. 4b).

Fig. 9 Hardness distribution from the edge of the punched hole



4.3.2 Microstructure After Hole Expansion Test

Figure 10 illustrates cross-sectional views and microstructural changes in DQP samples under HET. The HET process introduces a shear strain gradient through its thickness direction, leading to the development of shear flow bands [46–48](Fig. 10e). Shear flow bands expedite the TRIP effect, contributing to layered martensite/RA structure formation. Grains tend to align along the shearing direction, so rotated martensite laths with inter-lath films are arranged along shear flow lines (Fig. 10d). Also, it is well known that voids and microcracks initiate more easily at the martensite/austenite interface due to strain partitioning [49–51]. Figure 10b highlights an enlarged edge region above the red arrowed line, where most grains transformed into strain-induced martensite.

Nevertheless, it is important to acknowledge that the presence of strain induced martensite tends to diminish fracture resistance in subsequent HET. Figure 10g illustrates the zig-zag crack pattern in the hole expansion tested QP5-S10 sample. The distinctive zig-zag pattern on the crack surface is indicative of ductile failure, implying a ductile fracture mode in the QP5-S10 specimen.

QP5-S10 exhibits superior stretch flangeability compared to QP5 (refer to Fig. 4b). Figure 10 depicts the microstructural evolution of HET-tested QP5-S10, showing a lower fraction of RA and a reduced phase interface between soft and hard constituents compared to QP5. The substantial transformation of RA into martensite at the hole edge promotes microstructural homogeneity. This aligns with the findings of Yoon et al. [15, 52–54], suggesting that increased

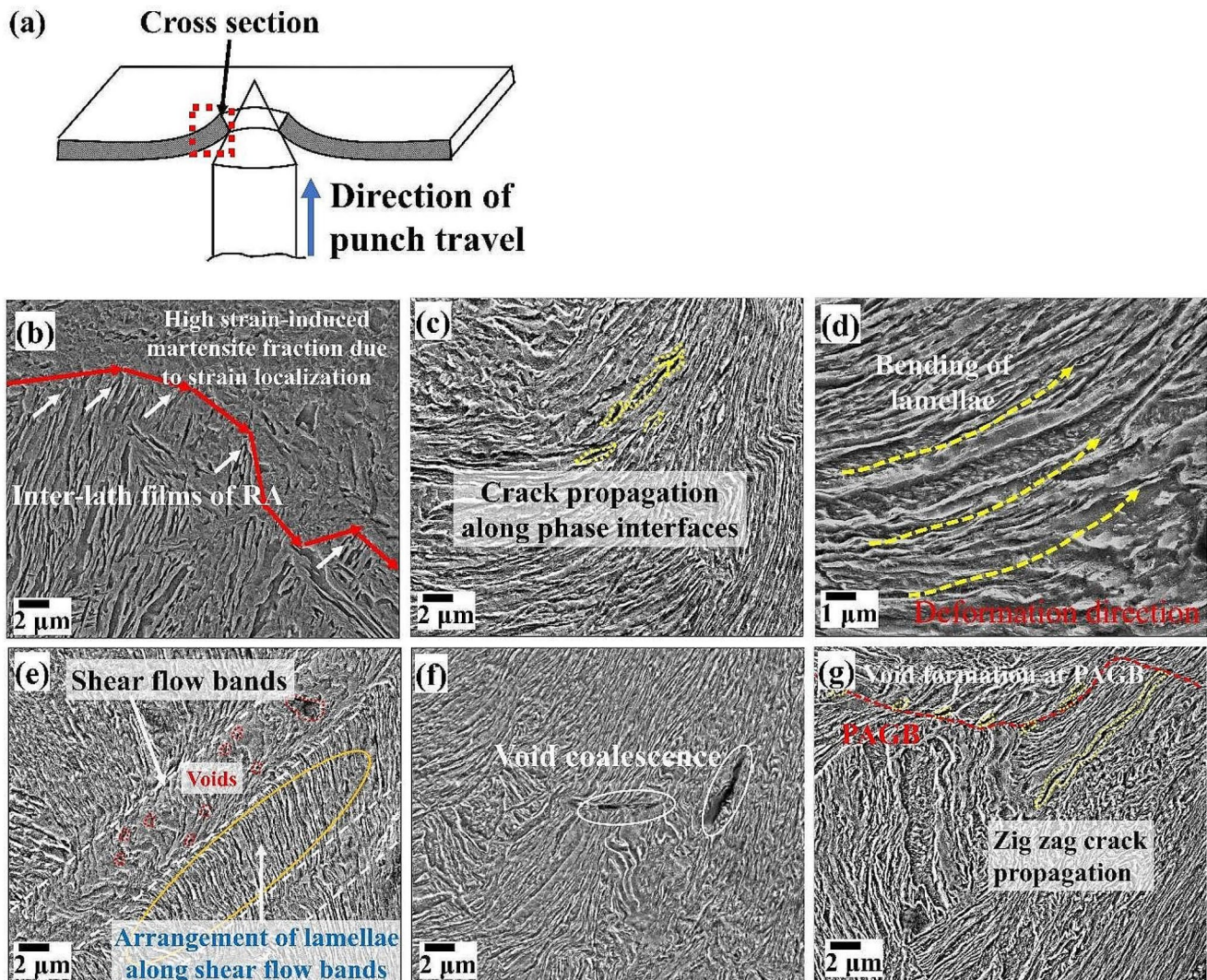


Fig. 10 Examination of microstructural changes at hole edges following hole expansion tests: (a) schematic illustrating the location for microstructure analysis on the hole expansion tested sample. SEM

micrographs showing the hole edge microstructure of (b) QP3, (c) QP3-S1, (d) QP3-S10, (e) QP5, (f) QP5-S1, and (g) QP5-S10

microstructural homogeneity enhances fracture toughness, ultimately improving stretch flangeability.

In earlier studies, defects such as microvoids and microcracks were found to predominantly develop in the SAZ during HET, particularly at the interfaces between soft and hard phases, owing to stress concentration and non-uniform strain distribution [55]. A comparison of the matrix structure in the QP5-S10 sample before deformation (see Fig. 6a) with the QP5 sample revealed uneven strain partitioning in the latter due to a higher fraction of phase interfaces, depicted by coarse fresh martensite or blocky RA islands (Figs. 2b and 8a). Kernel Average Misorientation (KAM) values at various distances from the punched hole edge, as summarized in Fig. 11, indicated a gradual decrease with distance from the initially punched hole, signifying sheared damage during punching. Additionally, greater KAM values in the same region of the QP5 sample compared to the QP5-S10 sample suggested a more rapid increase in the KAM value in SAZ. This finding implies that the lath martensite matrix with a substantial amount of coarse fresh martensite and blocky RA islands is more susceptible to severe plastic deformation, leading to more microvoids during the HET process.

Due to the distinct morphology of RA, void formation and crack initiation varied noticeably among DQP-processed steels. In the QP5-S10 sample, abundant lath martensite with a small fraction of RA contributed to improved microstructural homogeneity, contributing to a uniform strain distribution during HET. Simultaneously, the film-type RA in QP5-S10 effectively restrained crack formation and impeded crack propagation between martensite laths. Conversely, the QP5 sample, characterized by the presence of coarse fresh martensite or RA islands, exhibited comparatively higher hardness, causing an uneven distribution

of hardness at the phase interfaces. As strain increased, MA islands with high hardness struggled to maintain compatibility with the soft-tempered martensite, leading to voids and cracks at the phase interfaces. Moreover, large MA islands significantly increased the risk of crack formation, with cracks rapidly propagating and coalescing along the interface between MA islands and the tempered martensite matrix (Fig. 10). The QP5 sample shows several microvoids exhibiting smaller dimensions in length and width. Interestingly, in the QP5-S10 sample, despite having fewer voids, the microvoids displayed larger diameters and aspect ratios (Fig. 10g), contributing to a higher HER.

4.3.3 Global and Local Formability Ensured by Stable RA

The HER in single-step Q&P specimens is lower due to fresh martensite with high hardness and a significant fraction of blocky RA with lower stability. Previous research has demonstrated that RA grains with a blocky morphology are less stable during deformation than those with film-like morphology, even if the latter has a lower carbon content [41, 56]. Additionally, the large fresh martensite islands with high hardness are capable of initiating microcracks during HET. In contrast, secondary partitioned specimens exhibit a higher HER than single-step Q&P specimens, predominantly due to the significant improvement in RA stability. However, exceedingly stable RA obtained at shorter secondary partitioning times (QP3-S1 and QP5-S1) does not effectively contribute to deformation, leading to suboptimal HER. In contrast, longer partitioning times (QP3-S10 and QP5-S10) lead to the lower bainite formation, reducing carbon availability for RA enrichment, resulting in relatively lower stability than QP3-S1 and QP5-S1. Achieving an excellent combination of strength-ductility-formability

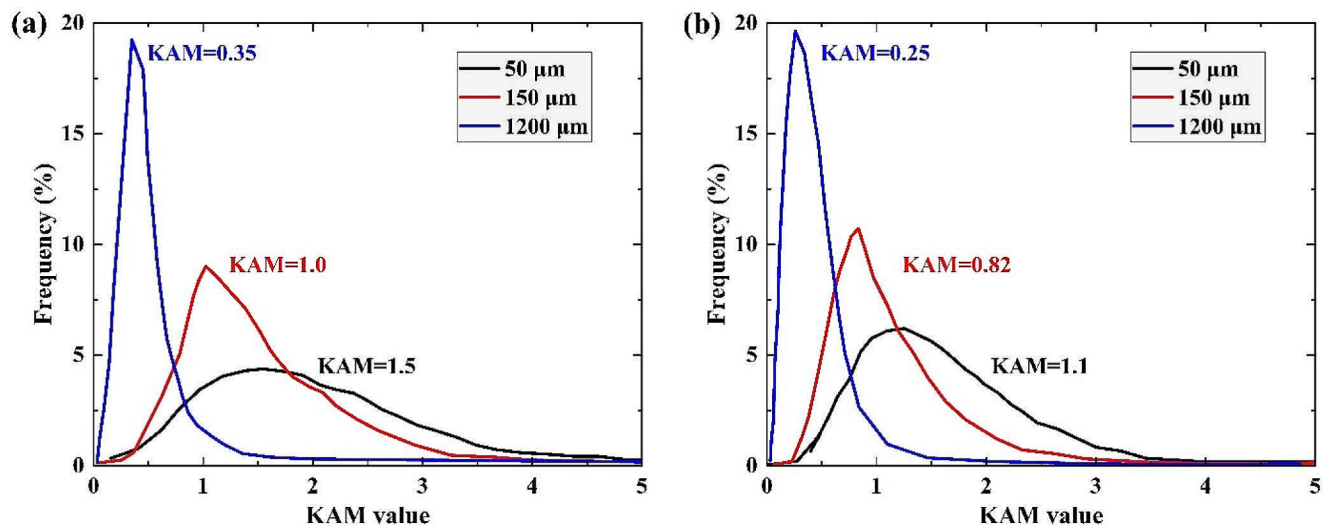
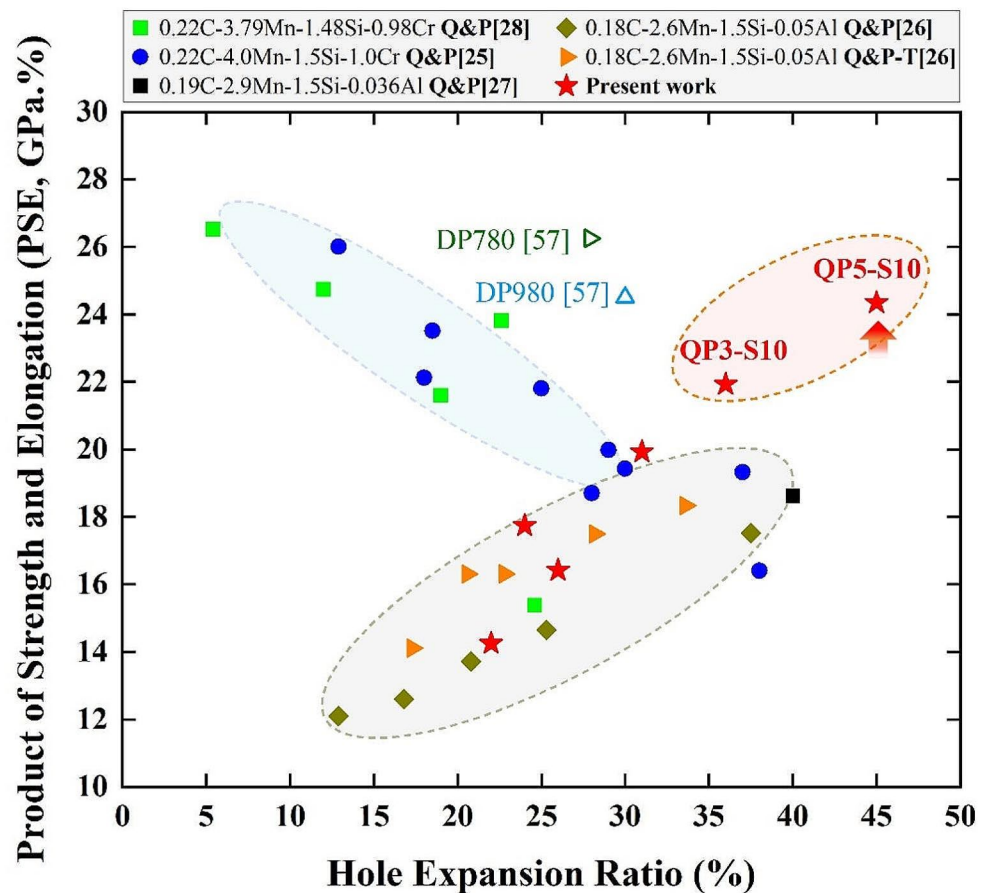


Fig. 11 KAM results for (a) QP5 and (b) QP5-S10 samples at various distances from punched hole edge

Fig. 12 The relationship between the hole expansion ratio (HER) and the product of strength and elongation (PSE, GPa.%). The results of the current study were compared to the reference results [25–28, 57] measured under similar test conditions (punched specimens and 60° conical punch)



in ultra high-strength Q&P steels depends on RA with adequate stability.

Figure 12 compares the HER values achieved in the current investigation to the HER values achieved under similar test conditions (punched specimens and 60° conical punch) from Refs. [25–28, 57]. Previous published literature has shown that AHSS with complex phases cannot always exhibit outstanding formability and elongation. However, our findings highlight that the introduction of secondary partitioning presents an effective means of achieving an excellent strength-ductility-formability combination (PSE = 24GPa.% and HER = 45%) of QP5-S10 placing it in prominent position on the PSE-HER map. The remarkable HER increase in QP5-S10 is attributed to the unique microstructure resulting from secondary partitioning.

5 Conclusions

In this work, the single-step DQP process and DQP with a secondary partitioning stage, is purposely designed to manipulate the stability of retained austenite. The effect of retained austenite stability on tensile properties and stretch

flangeability is investigated in detail, leading to the following conclusions.

- The introduction of secondary partitioning presents an effective means of achieving an excellent strength-ductility-formability combination (PSE = 24GPa.% and HER = 45%) in QP5-S10. The remarkable HER increase in QP5-S10 is attributed to the unique microstructure (matrix of tempered martensite and stable retained austenite, predominantly film-type along with small-sized blocky retained austenite) resulting from secondary partitioning.
- It is found that the introduction of secondary partitioning plays a critical role in the microstructure evolution and mechanical properties of the investigated steel. The size of the blocky retained austenite islands was found to play a dominating role in controlling its stability. Especially three types of retained austenite stabilities were identified: (i) unstable retained austenite comprising predominantly of larger size blocky type retained austenite islands, (ii) exceedingly stable retained austenite with the highest carbon content, which comprises primarily of film-type and does not effectively contribute to TRIP and (iii) stable retained austenite which is

predominantly film-type and along with small-sized blocky retained austenite islands. A stable retained austenite comprising predominantly film type along with small-sized blocky retained austenite is beneficial for an optimal strength-ductility-formability combination of the investigated steel.

- c. The current investigation introduces secondary partitioning into the Q&P process, thereby establishing a feasibility approach to control retained austenite characteristics affecting the retained austenite transformation activity. The retained austenite can be adequately stabilized and tuned by controlling the partitioning time. This allows for producing a large fraction of total retained austenite, predominantly film-type, along with small-sized blocky retained austenite islands, resulting in high-strength Q&P steels simultaneously achieving excellent global and local formability.

Acknowledgements This work was supported by the (i) National Research Foundation of Korea (NRF) grant funded by the Korea government (MSIP) [NRF-2021R1A2C3006662, NRF-2022R1A5A1030054], (ii) Center of Excellence in Steel Technology, IIT Madras (funded by Ministry of Steel, Govt of India), (iii) Department of Science and Technology, Govt. of India, through the sponsored project [Grant No. SP20211038MMSERB008277], (iv) Ministry of Education, Govt. of India, through the Institutes of Eminence for the research initiatives on establishing the IoE Research Centre for Advanced Microscopy and Materials [Grant No. SB20210844M-MMHRD008277] and (v) International Immersion Experience travel grant from IIT Madras.

Author Contributions Chintada Umasankar: Conceptualization, Methodology, Visualization, Data curation, Investigation, Validation, Formal analysis, Writing – original draft. Kali Prasad: Methodology, Data curation. Yeo Taek Choi: Methodology, Data curation. Do Won Lee: Methodology, Data curation. Hyong Seop Kim: Resources, Funding acquisition, Writing – review and editing. S. Sankaran: Supervision, Conceptualization, Writing – review and editing, Funding acquisition, Project administration. Uday Chakkingal: Supervision, Conceptualization, Writing – review and editing, Funding acquisition, Project administration.

Data Availability Data will be made available on request.

Declarations

Competing Interest The authors declare that they have no known competing financial interests or personal relationships that could have appeared to influence the work reported in this paper. Hyong Seop Kim is an Editor-in-Chief of Metals and Materials International.

References

- X. Tan, Y. Xu, X. Yang, D. Wu, *Mater. Sci. Eng. A* **589**, 101 (2014). <https://doi.org/10.1016/J.MSEA.2013.09.063>
- O. Tikhe, P. Doiphode, U. Nichul, R. Singh, V. Hiwarkar, *Met. Mater. Int.* **29**, 2216 (2023). <https://doi.org/10.1007/S12540-022-01375-6>
- N. Maheswari, S.G. Chowdhury, K.C. Hari Kumar, S. Sankaran, *Mater. Sci. Eng. A* **600**, 12 (2014). <https://doi.org/10.1016/j.msea.2014.01.066>
- M. Liu, J. Wang, Q. Zhang, H. Hu, G. Xu, *Met. Mater. Int.* **27**, 2473 (2021). <https://doi.org/10.1007/S12540-020-00726-5>
- T.Y. Hsu, X.J. Jin, Y.H. Rong, *J. Alloys Compd.* **577**, 568 (2013). <https://doi.org/10.1016/j.jallcom.2012.02.016>
- X. Gui, G. Gao, H. Guo, F. Zhao, Z. Tan, B. Bai, *Mater. Sci. Eng. A* **684**, 598 (2017). <https://doi.org/10.1016/j.msea.2016.12.097>
- J.H. Kim, M.H. Kwon, J.S. Lee, S. Lee, K. Lee, D.W. Suh, *ISIJ Int.* **61**, 518 (2021). <https://doi.org/10.2355/ISIJINTERNATIONAL.ISIJINT-2019-733>
- X. Tan, Y. Xu, X. Yang, Z. Liu, D. Wu, *Mater. Sci. Eng. A* **594**, 149 (2014). <https://doi.org/10.1016/j.msea.2013.11.064>
- R. Parthiban, S. Ghosh Chowdhury, K.C. Harikumar, S. Sankaran, *Mater. Sci. Eng. A* **705**, 376 (2017). <https://doi.org/10.1016/j.msea.2017.08.095>
- R. Parthiban, R.K. Ray, K.C. Hari kumar, S. Sankaran, *Mater. Sci. Eng. A* **825**, 141893 (2021). <https://doi.org/10.1016/j.msea.2021.141893>
- S. Chatterjee, H.K.D.H. Bhadeshia, *Mater. Sci. Technol.* **23**, 606 (2007). <https://doi.org/10.1179/174328407X179511>
- S. Sadagopan, D. Urban, C. Wong, M. Huang, B. Yan, *Formability characterization of a new Generation high strength Steels*, Technical Report (2003). <https://doi.org/10.2172/1001171>
- X. Chen, H. Jiang, Z. Cui, C. Lian, C. Lu, *Procedia Eng.* **81**, 718 (2014). <https://doi.org/10.1016/j.proeng.2014.10.066>
- J.H. Kim, Y.J. Kwon, T. Lee, K.A. Lee, H.S. Kim, C.S. Lee, *Met. Mater. Int.* **24**, 187 (2018). <https://doi.org/10.1007/S12540-017-7288-2>
- J.I. Yoon, J. Jung, H.H. Lee, G.S. Kim, H.S. Kim, *Met. Mater. Int.* **22**, 1009 (2016). <https://doi.org/10.1007/s12540-016-6346-5>
- J. Lee, S.J. Lee, B.C. De Cooman, *Mater. Sci. Eng. A* **536**, 231 (2012). <https://doi.org/10.1016/j.msea.2012.01.003>
- B.S. Levy, C.J. Van Tyne, *J. Mater. Eng. Perform.* **21**, 2147 (2012). <https://doi.org/10.1007/s11665-011-0116-9>
- S.K. Paul, *J. Mater. Eng. Perform.* **23**, 3610 (2014). <https://doi.org/10.1007/s11665-014-1161-y>
- K.I. Sugimoto, A. Nagasaka, M. Kobayashi, S.I. Hashimoto, *ISIJ Int.* **39**, 56 (1999). <https://doi.org/10.2355/isijinternational.39.56>
- K. Hasegawa, K. Kawamura, T. Urabe, Y. Hosoya, *ISIJ Int.* **44**, 603 (2004). <https://doi.org/10.2355/isijinternational.44.603>
- A. Karelou, C. Kremaszky, E. Werner, T. Hebesberger, A. Pichler, *Steel Res. Int.* **80**, 71 (2009). <https://doi.org/10.2374/SRI08SP110>
- K.I. Sugimoto, J. Sakaguchi, T. Iida, T. Kashima, *ISIJ Int.* **40**, 920 (2000). <https://doi.org/10.2355/isijinternational.40.920>
- E. De Moor, D.K. Matlock, J.G. Speer, C. Fojer, J. Penning, *Sae Tech. Pap.* **1**, 47 (2012). <https://doi.org/10.4271/2012-01-0530>
- P. Huyghe, S. Dépinoy, M. Caruso, D. Mercier, C. Georges, L. Malet, S. Godet, *ISIJ Int.* **58**, 1341 (2018). <https://doi.org/10.2355/isijinternational.ISIJINT-2018-121>
- J.H. Kim, S.W. Lee, K. Lee, J.K. Kim, D.W. Suh, *JOM.* **71**, 1366 (2019). <https://doi.org/10.1007/s11837-019-03332-y>
- Y.R. Im, E.Y. Kim, T. Song, J.S. Lee, D.W. Suh, *ISIJ Int.* **61**, 572 (2021). <https://doi.org/10.2355/isijinternational.ISIJINT-2020-388>
- Y. Toji, T. Nakagaito, H. Matsuda, K. Hasegawa, S. Kaneko, *ISIJ Int.* **63**, 758 (2023). <https://doi.org/10.2355/isijinternational.ISIJINT-2022-508>
- J.H. Kim, E.J. Seo, M.H. Kwon, S. Kang, B.C. De Cooman, *Mater. Sci. Eng. A* **729**, 276 (2018). <https://doi.org/10.1016/j.msea.2018.05.083>
- H. Carvalho Ferreira, F. Jose Martins Boratto, V. Tadeu Lopes, Buono, *Mater. Sci. Eng. A* **628**, 110 (2015). <https://doi.org/10.1016/j.msea.2015.01.019>

30. N.H. Van Dijk, A.M. Butt, L. Zhao, J. Sietsma, S.E. Offerman, J.P. Wright, S. Van Der Zwaag, *Acta Mater.* **53**, 5439 (2005). <https://doi.org/10.1016/J.ACTAMAT.2005.08.017>
31. M.J. Santofimia, L. Zhao, R. Petrov, J. Sietsma, *Mater. Charact.* **59**, 1758 (2008). <https://doi.org/10.1016/J.MATCHAR.2008.04.004>
32. ASTM E8/E8M-22, Standard Test Methods for Tension Testing of Metallic Materials (ASTM International, West Conshohocken, 2022). https://www.astm.org/e0008_e0008m-22.html, Accessed 5 May 2024
33. H.S. Kim, J.I. Yoon, H.H. Lee, J. Jung, Method of evaluating stretch-flangeability with small-scale specimen without specimen size effects, US Patent 10274407 (2019). <https://patents.google.com/patent/US10274407B2/en>
34. J.I. Yoon, J. Jung, H.H. Lee, H.S. Kim, J.O.M.-J. Miner, *Met. Mater. Soc.* **70**, 912 (2018). <https://doi.org/10.1007/s11837-018-2766-7>
35. ISO 16630, Metallic Materials-Sheet and Strip-Method of Hole Expanding Test (International Organization for Standardization, Switzerland, 2009). <https://www.iso.org/standard/69771.html>
36. M.J. Santofimia, L. Zhao, R. Petrov, C. Kwakernaak, W.G. Sloof, J. Sietsma, *Acta Mater.* **59**, 6059 (2011). <https://doi.org/10.1016/J.ACTAMAT.2011.06.014>
37. K. Sugimoto, M. Kobayashi, S.-I. Hashimoto, *Metall. Mater. Trans. A* **23**, 3085 (1992). <https://doi.org/10.1007/BF02646127>
38. P.J. Jacques, F. Delannay, J. Ladrière, *Metall. Mater. Trans. A* **32**, 2759 (2001). <https://doi.org/10.1007/S11661-001-1027-4>
39. P.J. Jacques, Q. Furnémont, F. Lani, T. Pardoën, F. Delannay, *Acta Mater.* **55**, 3681 (2007). <https://doi.org/10.1016/J.ACTAMAT.2007.02.029>
40. C. Song, H. Yu, L. Li, T. Zhou, J. Lu, X. Liu, *Mater. Sci. Eng. A* **670**, 326 (2016). <https://doi.org/10.1016/j.msea.2016.06.044>
41. X.C. Xiong, B. Chen, M.X. Huang, J.F. Wang, L. Wang, *Scripta Mater.* **68**, 321 (2013). <https://doi.org/10.1016/j.scriptamat.2012.11.003>
42. Z. Xiong, P.J. Jacques, A. Perlade, T. Pardoën, *Metall. Mater. Trans. A* **50**, 3502 (2019). <https://doi.org/10.1007/s11661-019-05265-2>
43. L. Liu, B.B. He, G.J. Cheng, H.W. Yen, M.X. Huang, *Scripta Mater.* **150**, 1 (2018). <https://doi.org/10.1016/j.scriptamat.2018.02.035>
44. E.J. Seo, L. Cho, Y. Estrin, B.C. De Cooman, *Acta Mater.* **113**, 124 (2016). <https://doi.org/10.1016/j.actamat.2016.04.048>
45. C. Zhang, Z. Xiong, D. Yang, X. Cheng, *Acta Mater.* **235**, 118060 (2022). <https://doi.org/10.1016/j.actamat.2022.118060>
46. N. Triantafyllidis, A. Needleman, V. Tvergaard, *Int. J. Solids Struct.* **18**, 121 (1982). [https://doi.org/10.1016/0020-7683\(82\)90021-X](https://doi.org/10.1016/0020-7683(82)90021-X)
47. M. Kuroda, V. Tvergaard, E.J. Mech, *A-Solid.* **23**, 811 (2004). <https://doi.org/10.1016/J.EUROMECHSOL.2004.05.006>
48. J. Ma, T. Welo, I.J. Mach, *Tools Manuf.* **160**, 103653 (2021). <https://doi.org/10.1016/J.IJMACHTOOLS.2020.103653>
49. D. Hull, D.E. Rimmer, *Philos. Mag.* **4**, 673 (1959). <https://doi.org/10.1080/14786435908243264>
50. Y. Yang, H. Wang, C. Wang, L. Yang, *Steel Res. Int.* **91** (2020). <https://doi.org/10.1002/SRIN.201900583>
51. J.I. Yoon, J. Jung, J.H. Ryu, K. Lee, H.S. Kim, *Exp. Mech.* **57**, 1349 (2017). <https://doi.org/10.1007/s11340-017-0306-y>
52. J.I. Yoon, J. Jung, H.H. Lee, J.Y. Kim, H.S. Kim, *Met. Mater. Int.* **25**, 1161 (2019). <https://doi.org/10.1007/s12540-019-00270-x>
53. J.I. Yoon, J. Jung, J.G. Kim, S.S. Sohn, S. Lee, H.S. Kim, *J. Mater. Sci.* **52**, 7808 (2017). <https://doi.org/10.1007/s10853-017-1012-y>
54. J.I. Yoon, H.H. Lee, J. Jung, H.S. Kim, *Mater. Sci. Eng. A* **735**, 295 (2018). <https://doi.org/10.1016/j.msea.2018.08.052>
55. Y. Wang, Y. Xu, Y. Wang, J. Zhang, C. Guo, X. Wang, W. Zhao, H. Liu, *J. Mater. Res. Technol.* **26**, 5503 (2023). <https://doi.org/10.1016/J.JMRT.2023.08.226>
56. D. De Knijf, R. Petrov, C. Föjler, L.A.I. Kestens, *Mater. Sci. Eng. A* **615**, 107 (2014). <https://doi.org/10.1016/j.msea.2014.07.054>
57. J.I. Yoon, J. Jung, S.H. Joo, T.J. Song, K.G. Chin, M.H. Seo, S.J. Kim, S. Lee, H.S. Kim, *Mater. Lett.* **180**, 322 (2016). <https://doi.org/10.1016/j.matlet.2016.05.145>

Publisher's Note Springer Nature remains neutral with regard to jurisdictional claims in published maps and institutional affiliations.

Springer Nature or its licensor (e.g. a society or other partner) holds exclusive rights to this article under a publishing agreement with the author(s) or other rightsholder(s); author self-archiving of the accepted manuscript version of this article is solely governed by the terms of such publishing agreement and applicable law.